

A Fully Compressible, Two-Dimensional, Model of Small, High Speed, Cavitating Nozzles

David P. Schmidt, Christopher J. Rutland, and M. L. Corradini

Engine Research Center

University of Wisconsin, Madison

Keywords: cavitation, nozzle, fuel injection, compressible flow, CFD

Abstract

A numerical model that treats liquid and vapor as a continuum has been constructed for predicting small scale, high speed, cavitating, nozzle flow. In order to model extremely high pressures, the compressibility of both phases has been included in the scheme, and a third-order shock capturing technique was applied to the continuity equation to capture sharp jumps in density. In addition, a boundary-fitted mesh was used to treat different nozzle geometries. The scheme has been run with very high upstream pressures and with a liquid to vapor density ratio of ten-thousand to one. The model results have been compared to experimental measurements of single bubble collapse. Results are also presented for rounded and sharp nozzle entrances with varying upstream pressures. The model successfully predicted coefficient of discharge and exit velocity for a variety of nozzle geometries.

Introduction

Nozzles are one of the most fundamental devices in fluid mechanics. Small, high-speed nozzles are used in numerous industrial applications such as engines and liquid cutting jets. In the case of engines, fuel injector nozzles are a critical starting point for fuel dispersion and combustion. Unfortunately, very little is known about the internal flow through high pressure injector nozzles, because the nozzles are very small and the flow is very fast. In industrial and engine applications, injection pressures can be in excess of 150 MPa with nozzle diameters on the order of 200 microns. The internal nozzle flow can reach speeds over 500 m/s. This combination of high speed and small size makes experimental measurements of the flow extremely difficult. The nozzle flow cannot be easily scaled up for experimental study, because the flow is described by a large number of parameters, many of which involve fluid properties. To further the understanding of cavitating nozzles, a numerical model of very high-speed cavitating flow has been constructed.

This physical situation at such high injection pressures is quite extreme in several respects. The Mach number based on the sound speed of liquid can exceed 0.4, which suggests that the liquid compressibility could be significant. Also, the length scale of this geometry is so small that individual cavitation bubbles could span several computational cells. The density ratio between the two phases is very large, roughly ten-thousand to one. By comparison, the density ratio across a shock in aerodynamic problems is usually an order of ten or less. These factors tend to make this a particularly challenging problem to model. Special steps are required to ensure stability when modeling a large change in density over the space of a few computational cells.

Past attempts to numerically model cavitating flow can be roughly divided into two classes: interface tracking and continuum methods. Interface tracking is a promising numerical technique for two-phase flows. In this case each phase is treated separately. There are typically separate equations for conservation of mass and momentum of each phase, which more than doubles the computational cost of modeling the flow. Furthermore, a scheme for reconstructing the interface on the sub-cell level is required. This reconstruction can be based on marker particles or heuristics

for modeling the interface on the sub-cell level (Hyman, 1984). Rider and Kothe (1995) have shown the computational cost of interface tracking schemes to be at least six times the cost of continuum methods. They also noted that they have been applied to density ratios of, at most, one-thousand to one.

The model presented in this paper is a continuum method, where the two phases are considered to be the same fluid. The interface is smeared on the sub-cell level, and the density reflects the cell's liquid and vapor content. Often, surface tension forces are neglected in continuum methods, since a distinct interface is not present. The continuum method is a convenient way of mathematically modeling the flow, because it requires no more equations than single-phase flow. The difficult part of developing such models is deriving a meaningful and stable equation for pressure. The works of Kubota et al. (1989), Delannoy and Kueny (1990), and Chen and Heister (1994), and Avva et al. (1995) are all examples of continuum methods.

Kubota et al. developed one of the earliest continuum models of cavitating flow. However they developed a constitutive relation for pressure based on the assumption that the fluid was a uniform mixture of liquid and very small, spherical bubbles. Kubota et al. used relations for bubble radius, average cell density, and pressure to close the set of equations. They noted the extreme density ratio between the liquid and vapor and thus chose to neglect the mass of the vapor. The authors encountered severe stability problems and were limited to moderate void fractions. Because of the stability limitations and the assumptions of this constitutive relation, this approach is not appropriate for small, high speed, nozzles.

Delannoy and Kueny used a simpler method for closure of the hydrodynamic equations. They assumed a barotropic equation of state where density was a function of pressure. The two constant densities were joined by a sine function whose maximum slope was chosen to roughly represent the speed of sound of a two-phase mixture. A plot of this equation of state is shown in Figure 1. Delannoy and Kueny used a shock capturing technique to improve the stability of their code but

were limited to density ratios of one hundred to one. Their scheme was based on the SIMPLE algorithm, which models incompressible flows (Delannoy, 1989). They presented results for modeling a large, cavitating venturi. Delannoy and Kueny achieved qualitatively reasonable results, although they did not quantitatively match experimental data. They predicted a cavity that was double the experimentally measured length. Their model also under-predicted shedding frequency of the cavitation bubble by about forty percent.

The inaccurate predictions of Delannoy and Kueny may be due to the smearing of the fluid interface over at least one cell length by the continuum treatment. Also, the continuum treatment of the two phases usually assumes that there is no inter-phase slip on the sub-cell level. This requires an inter-phase drag force that may not, in reality, be present. These limitations would occur in almost any continuum treatment and usually require a fine computational mesh. Also Delannoy and Kueny solved the Euler equations rather than the Navier-Stokes equations and so they may not have accurately predicted the near-wall flow. Another problem with their calculation was their density ratio. Rather than using a realistic liquid to vapor density ratio of $1:10^{-5}$, Delannoy and Kueny used a ratio of $1:10^{-2}$. Lastly, it may not be possible to predict such refined details as shedding frequency in two-dimensions since the bubble collapse at the end of a cavity is essentially three-dimensional.

Later work by Chen and Heister (1995) rejected the idea of a simple one-to-one mapping of pressure and density. They argued that the pressure field should be related to the density history. However, Chen and Heister had to make several assumptions to develop an equation for pressure. They assumed that the bubble number per unit mass was constant and that each cell was uniformly filled with small, spherical bubbles. This solution technique is somewhat reasonable for large scale flows, but does not seem realistic for very small nozzles, where the individual bubble size could be considerably larger than a computational cell.

Avva et al. (1995) used an energy equation for closure and thus avoided the need for developing a new constitutive relation. They started with an energy equation for a two-phase mixture. The authors then assumed homogenous flow, no slip, and thermodynamic equilibrium. With these assumptions, the energy equation was simplified to a single fluid energy equation based on a mean cell density. The model was tested in sharp-edged orifice calculations and for flow around a hydrofoil. The results agreed reasonably well with experimental results, however the authors reported problems with the model's stability. They were unable to simulate cold fluid flow and were forced to increase the fluid temperature to 354.5 K which reduced the ratio of liquid to vapor density to three thousand. The model was also limited to very low upstream pressures due to stability problems.

One important limitation of all these studies is that the pure phases were considered to be incompressible. The current model, described in the next section, considers the compressibility of both pure phases. This phenomenon allows for the study of wave motion in the fluid, an impossibility in the previous work. Compressibility is known to become significant in the latter stages of bubble collapse and has been studied using one-dimensional models (Knapp, 1970). The model presented here makes further assumptions, which are valid for small scale, high speed flows. Thermal non-equilibrium effects will be neglected, as will hydrodynamic non-equilibrium. The resulting problem is hyperbolic, unlike any of the previously reviewed work in multi-dimensional cavitation modeling.

Model Physics

The first step in formulating the numerical model of high-speed cavitating flow is to identify the important physical processes. Many phenomena can be evaluated by an order of magnitude analysis. For example, the Weber number for this flow is estimated to be about $4 \cdot 10^4$, which indicates that surface tension forces are negligible. The high Reynolds number of the nozzle flow, on the order of 10^5 , indicates that the flow is turbulent. However, cavitation is a much more violent phenomenon than turbulence. Moreover the prediction of turbulence in cavitating flow is

most likely beyond the scope of current turbulence models. Hence, no turbulence model is included in the present work. For more discussion of turbulence in cavitating nozzles, the reader should refer to He and Ruiz (1995).

The most crucial part of modeling cavitating flow is the closure of the hydrodynamic equations. The type of closure used by Kubota et al. (1989) and Chen and Heister (1995) does not seem appropriate for extremely small nozzles. In both of these studies the authors assumed homogenous, sub-grid scale, bubble distributions. For such a small-scale flow the energy equation used by Avva et al. (1995) appears to be a more appropriate starting point. Equation 1 is a conservation of energy statement assuming homogenous equilibrium of the two phases and includes the viscous dissipation term, Φ .

$$\rho \frac{Dh}{Dt} = \frac{DP}{Dt} + \nabla k \nabla T + \Phi \quad (1)$$

The order of magnitude of each term is estimated using values that are appropriate for 100 MPa injection of fuel through nozzles with a diameter of 200 microns, and a density of 860 kg/m³. Rough estimates of enthalpy, thermal conductivity, and temperature difference are 2500 kJ/kg, 0.613 W/m*K, and 30 K, respectively. Using these figures, the enthalpy and pressure work term are at least five orders of magnitude greater than the conduction and viscous terms. These estimates suggest that thermal conduction and viscous work can be neglected from the energy equation. Because these terms, which are associated with irreversibilities, are found to be negligible, the reduced energy equation admits only pressure work and enthalpy storage:

$$\rho \frac{Dh}{Dt} = \frac{DP}{Dt} \quad (2)$$

Thus it is assumed that the mechanical driving force due to the upstream pressure is much larger than any thermal effect or viscous losses. The remaining terms describe reversible work and suggest that in place of the energy equation one may use an isentropic model equation.

$$a^2 \frac{D\rho}{Dt} = \frac{DP}{Dt} \quad (3)$$

As mentioned previously, the Mach number based on the liquid sound speed for high speed nozzle flow is approximately 0.4. The Mach number based on a two-phase sound speed or on the vapor sound speed would be much higher. These Mach numbers indicate that the numerical scheme

should include compressibility effects. As an additional advantage compressibility should enhance calculation of bubble collapse (Knapp, 1970). Also, it seems likely that the inclusion of compressibility effects could improve the stability of the numerical scheme by allowing compressive energy storage. A simple analysis based on sound speed and the continuity equation can quantify this benefit. Consider isentropic compression of a fluid in an Eulerian reference frame:

$$\frac{D\rho}{Dt} = \frac{1}{a^2} \frac{Dp}{Dt} \quad (4)$$

Expanding the continuity equation using the product rule gives:

$$\frac{\partial \rho}{\partial t} + \vec{V} \cdot \vec{\nabla} \rho + \rho \vec{\nabla} \cdot \vec{V} = 0 \quad (5)$$

Substitution of Eqn. 4 into Eqn. 5 eliminates the substantial derivative of density and instead relates the pressure change to the velocity divergence:

$$\frac{Dp}{Dt} = -a^2 \rho \vec{\nabla} \cdot \vec{V} \quad (6)$$

If the pure liquid phase is treated as incompressible, then a becomes infinite at the moment of bubble collapse. So at the end of bubble collapse the velocity divergence must instantly go to zero or else the pressure response is infinite. However, if the velocity divergence discontinuously goes to zero then there is an infinite acceleration that also could cause an infinite pressure response. By allowing for liquid compressibility, the fluid can naturally absorb the kinetic energy of bubble collapse and the pressure remains bounded.

Two-Phase Thermodynamics

Though these simplifying assumptions are certainly applicable for the liquid phase, one would prefer additional confirmation of the applicability to two-phase flow. Eqn. 3 would represent cavitation as an inertially dominated process, with negligible thermodynamic effects. This is a common assumption, because the heat transfer from a bubble to the surrounding liquid takes place on length scales that are on the order of microns and is very rapid. According to Knapp et al. (1970) the heat transfer in cold fluids is usually so fast that it may be considered instantaneous.

In order to further verify this assumption, the criterion of Kato et al. (1994) is used. Kato et al. compared the growth of an axisymmetric, inertially driven, bubble to the growth of a thermally driven bubble. They used the asymptotic behavior of an inertial and thermal model to compare bubble radii. The asymptotic solution for the radius of an inertially driven bubble was given as:

$$R_I = \sqrt{\frac{2\Delta p}{3\rho_l}t} \quad (7)$$

where the pressure difference, Δp , is the pressure difference between the inside and outside of the bubble. The thermally driven asymptotic solution for bubble radius was given as:

$$R_T = Ja \sqrt{\frac{12\alpha t}{\pi}} \quad (8)$$

where Ja is the Jakob number and α is the thermal diffusivity. The Jakob number, $Ja = \rho_l C_p \Delta T / \rho_v L$, which represents the ratio of heat available from the surrounding liquid to the energy required for phase change, is estimated to be about 1250. It is assumed that inertial or thermal growth will limit growth based on which one would correspond to a smaller bubble at a given time, t . Since the radius of the inertial bubble grows linearly with time, but the radius of the thermal bubble grows with the square root of time, the inertial effects will initially dominate the bubble growth. At some later time, thermal effects will be important and begin to limit growth. This will occur when $R_T \leq R_I$. These two radii are equal when

$$t = 18 \frac{\rho_l Ja^2 \alpha}{\pi \Delta p} \quad (9)$$

Using 100 MPa for Δp , the thermal effects will not limit growth until the bubble has grown for 13 μ s at which point it would be 3mm in radius, which is much larger than the nozzles considered in this paper. This estimate is very conservative, since Kato et al. used estimates of roughly 2 kPa for Δp . Clearly, the geometry is too small and the flow is too fast for thermal non-equilibrium effects to be important.

In summary, the energy equation has been reduced based on an order of magnitude analysis. The assumption of thermodynamic equilibrium has been further validated using an asymptotic analysis reported by Kato et al. This closure along with the continuum treatment leads us to a barotropic equation of state, similar to Delannoy and Kueny. However our treatment differs in two important

respects: (1) The model is applied to very small scale calculations and very high velocities and (2) The compressibility of the liquid and vapor is included in a more rigorous manner. One of the known drawbacks of a barotropic equation of state is that it allows gradual density changes in the presence of gradual pressure changes. In the case of small, high-speed nozzles, the huge pressure gradients and small length scale reduces this limitation, as will be demonstrated by the results. The inertial non-equilibrium arguments of Chen and Heister are partially obviated because of the very small scale of these calculations. With grid cells only a few microns wide some of the small scale inertial effects should be represented in our calculation. One should take these concerns as warning not to apply this model to large scale, low speed cavitation calculations.

The Simplified Equation of State

Equation 3 may be considered an isentropic model of the phase change, where the speed of sound is given by the homogenous equilibrium model (HEM). This is modeled by

$$dp = a^2 d\rho \quad (10)$$

where a is given by Wallis(1969) as

$$a = \sqrt{\frac{1}{(\alpha \cdot \rho_g + (1 - \alpha)\rho_l) \cdot \left(\frac{\alpha}{\rho_g \cdot a_g^2} + \frac{(1 - \alpha)}{\rho_l \cdot a_l^2} \right)}} \quad (11)$$

The values of a_g and a_l are the sound speeds of the pure phases. In this expression, α is the void fraction and is given by

$$\alpha = \frac{\rho - \rho_l}{\rho_g - \rho_l} \quad (12)$$

By assuming constant sound speeds for the saturated vapor and liquid, the pressure may be analytically integrated as a function of void fraction. Integrating from the saturated liquid state gives:

$$p = p_l^{sat} + p_{gl} \cdot \log \left[\frac{\rho_g \cdot a_g^2 \cdot (\rho_l + \alpha \cdot (\rho_g - \rho_l))}{\rho_l \cdot (\rho_g \cdot a_g^2 - \alpha \cdot (\rho_g \cdot a_g^2 - \rho_l \cdot a_l^2))} \right] \quad (13)$$

where p_{gl} is not a function of void fraction, but rather a parameter of the fluid properties:

$$p_{gl} = \frac{\rho_g \cdot a_g^2 \cdot \rho_l \cdot a_l^2 \cdot (\rho_g - \rho_l)}{\rho_g^2 \cdot a_g^2 - \rho_l^2 \cdot a_l^2} \quad (14)$$

So pressure is given by an analytic function of density that is linear for pure liquid or vapor and is given by Eqn. 13 in the two-phase region, where $\rho_g < \rho < \rho_l$. Pressure according to this relationship is shown as a function of density in Fig. 1. This closure means that no partial differential equation is required for pressure. The pressure can be found analytically from the cell density which dramatically reduces the computational cost of a time step.

Numerical Solution

This model may be written as three partial differential equations and one algebraic equation of state:

$$\frac{\partial \rho}{\partial t} + \vec{\nabla} \cdot \rho \vec{V} + \omega H_\rho = 0 \quad (15)$$

$$\frac{\partial \rho u}{\partial t} + \vec{\nabla} \cdot \rho u \vec{V} + \omega H_x = -\frac{\partial p}{\partial x} + \nabla \mu \nabla u + \omega H_{xv} \quad (16)$$

$$\frac{\partial \rho v}{\partial t} + \vec{\nabla} \cdot \rho v \vec{V} + \omega H_y = -\frac{\partial p}{\partial y} + \nabla \mu \nabla v + \omega H_{yv} \quad (17)$$

$$p = p(\rho) \quad (18)$$

Equation 18 refers to Eqn. 13 or to the integral of Eqn. 10, depending on the cell density. In Eqns. 15, 16, and 17, ω is zero for calculations in Cartesian coordinates and unity for calculations in polar coordinates. In polar calculations, z replaces x and r replaces y . The convective and viscous axisymmetric source terms for polar calculations are:

$$\vec{H} = \begin{bmatrix} \frac{\rho v}{r} \\ \frac{\rho u v}{r} \\ \frac{\rho v^2}{r} \\ \frac{\rho v^2}{r} \end{bmatrix} \quad \vec{H}_v = \begin{bmatrix} 0 \\ \frac{\tau_{zr}}{r} \\ \mu \frac{\partial \left(\frac{\rho v}{r} \right)}{\partial r} \end{bmatrix} \quad (19),(20)$$

The interaction between velocity divergence and viscosity has been neglected, and an incompressible form of the shear terms was used, as in Chen and Heister (1994). The viscosity

was assumed to be linearly proportional to density for simplicity. Once the equations are non-dimensionalized, the viscosity appears as the density divided by the Reynolds number.

Equations 15, 16, and 17 are transformed to general (η, ζ) coordinates and solved in strong conservation form. These equations are solved on a staggered grid using third-order Runge-Kutta time stepping. All spatial derivatives are second-order central differenced. Thermodynamic variables are located at cell centers, metrics and velocities are defined at vertices, and contravariant velocities are defined at cell sides. Fourth-order viscosity is added to the velocities to smooth out the effect of the non-conservative axisymmetric terms and to complement the very low molecular viscosity. In each Runge-Kutta sub-step, the right-hand side of Eqn. (15) is calculated and the density is updated. This allows the pressure to be updated using Eqn. (18). Next, the right hand side of Eqns. (16) and (17) are evaluated and the velocities are updated. Finally, the boundary conditions are enforced and the fourth-order viscosity is added to the velocities. This algorithm requires no iterative pressure solution and thus avoids the cost and convergence problems of elliptic pressure solvers.

The model is typically run at a Reynolds number of 15,000 and uses a coefficient of fourth order viscosity of 0.05 for high speed runs and 0.01 or less for low speed runs. The calculations are non-dimensionalized using a reference pressure of 100 MPa, a density of 860 kg/m³, and a length scale of 200 μ m. The non-dimensional sound speeds for liquid and vapor are 3.5 and 0.9, respectively. Since this is an explicit scheme, the time step is limited by the speed of sound and local velocity. As a result, the code performs best at moderate Mach number and poorly at very low Mach number.

The key issue in the numerical solution of this system of equations is the resolution of the rapid density change across phases. The stability problems of cavitation calculations are much more severe than single-phase calculations. For example, the density ratio across an aerodynamic shock is typically an order of ten or less. In a cavitation calculations density must rapidly drop from a

value of about 1.0 (liquid density) to around 10^{-5} (vapor density) without ever reaching zero. Thus, a third order monotone shock capturing scheme is used. This scheme, published by Zijlema (1996), is applied only to the continuity equation, since the momentum equations already have fourth-order smoothing applied to them and are well behaved. This shock capturing technique uses a “flux limiter” to linearly combine the upwind and central difference operators. The flux limiter is given by

$$\Psi(r) = \frac{1}{2}(r + |r|) \frac{r + 3}{(1 + r)^2} \quad (21)$$

where r is the ratio of successive density gradients.

To further ensure stability, the density is checked at each sub-step and reset to 10^{-9} if it falls below this number. Though this violates conservation of mass, the magnitude of the correction is much smaller than the discretization error of the finite difference scheme. The total mass correction over time is reported by the model and is on the order of 0.01% of the nozzle mass flow rate. This correction is a necessary precaution when calculating mass flow in more than one spatial dimension, where shock capturing does not always demonstrate monotone behavior.

Boundary Conditions

The typical physical nozzle geometry is shown in Fig. 2 along with the computational domain. The left boundary is the inlet, representing a high pressure source of fluid. Flow exits the domain at the right boundary, which usually represents a large chamber. The top of the domain is a curved wall, and the bottom of the domain is a line of planar or axi-symmetry.

The use of the staggered grid makes boundary conditions on the wall and centerline very simple: the velocity at the wall is zero and v and is zero at the centerline. No explicit boundary conditions are required for the density because the densities are located a half-cell away from the boundaries, and the mass flux into the continuity cells from these boundaries is zero. For solving the u -momentum equation at the center line, symmetry is used to evaluate density.

The inlet boundary condition is computed in a simple fashion that is very useful for nozzle flows. Far upstream of the inlet the fluid has a negligible velocity and a specified stagnation state. The inlet boundary condition connects the interior to the stagnation conditions by a conservation of energy equation and an interpolation between the nearest point and the far-field. Equation 22 shows how the inlet pressure, p_{in} , is interpolated using the far-field pressure, p_0 , and the nearest cell pressure, p_1 . Equation 23 relates the far-field pressure and density, ρ_0 , to the velocity magnitude at the inlet boundary. The inlet velocity calculation requires a direction as well as a magnitude and so the velocity is constrained to be perpendicular to the inlet. Eqns. 18, 22, and 23 are solved at each cell vertex and cell side at the inlet boundary.

$$p_{in} = \frac{(p_0 + p_1)}{2} \quad (22)$$

$$\frac{p_0}{\rho_0} = \frac{p_{in}}{\rho_{in}} + \frac{u^2 + v^2}{2} \quad (23)$$

The outlet boundary condition is considerably more sophisticated, in order to deal with the compressible, two-phase nature of the flow. This boundary must let acoustic waves from the interior out of the domain without reflecting them. This boundary also must let bubbles out of the domain and be stable under a wide range of Mach numbers. Finally, the exit boundary represents the specified downstream pressure. An analysis similar to Thompson(1987) and Poinso and Lele(1992) is used to construct the finite difference equations. The flux terms normal to the exit are split into four characteristic waves given by an eigenfunction analysis. For supersonic conditions all the waves are moving from the domain outward, and derivatives normal to the exit are calculated using upwind differencing. Supersonic flow typically occurs when a cell contains both liquid and vapor, resulting in a very low sound speed. For the flow of pure liquid the exit is generally subsonic and one of the characteristic waves must be specified. Ideally this wave is specified in such a way that the exit is not entirely reflective, yet enforces the downstream pressure. The approach suggested by Poinso and Lele (1992) is used, where the incoming wave is assumed to be of the form:

$$\ell_1 \propto \kappa(p_{exit} - p_\infty) \quad (24)$$

ℓ_1 is the incoming characteristic wave that transmits the downstream pressure back into the domain. p_{exit} is the current pressure at the boundary between a cell and the exit, while p_∞ is the specified downstream pressure. κ is a constant chosen to be 0.05 for reasonable exit behavior. Poinso and Lele (1992) discussed how to estimate this number. As κ increases the exit pressure becomes more strongly tied to the specified downstream pressure but the boundary also becomes more reflective. The boundary lets the downstream pressure vary slightly from the specified downstream pressure. This treatment allows structures such as waves and bubble to pass through the exit without reflecting. The disadvantage of this exit boundary is that a value for κ must be specified, which can effect the solution.

In the case where flow at the exit is reversed two additional waves must be specified. In this case the incoming flow is assumed to be liquid moving normal to the exit boundary. This is not an accurate assumption for discharge into a gaseous environment, but is rather representative of a submerged nozzle. This is a limitation of the model due to the neglect of non-condensable gasses whose effect is not considered in the equation of state. This limitation precludes the code from predicting “hydraulic flip.” (Soteriou et al., 1995)

Once all four characteristic waves are determined, they are recombined to find the flux normal to the exit plane. Then the transverse and viscous terms of the governing equations are calculated. At this point, the density and velocity values are be updated on the downstream boundary. Finally, pressure is updated using Eqn. (18).

Results

The new cavitation model has been used for several different types of calculations. The collapse of a single bubble has been simulated as part of the model validation. The code was applied to a simple nozzle geometry in order to further validate the model as well as to learn about the behavior of cavitating nozzles. As a demonstration of other uses for the model, the flow through an

axisymmetric fuel injector tip was calculated. In order to investigate the effect of asymmetry on nozzle cavitation, the asymmetric flow through a slot was also predicted.

Although the nozzle calculations are the motivation for this effort, single bubble calculations can help to evaluate the model. By comparing the predicted rate of collapse to experimental measurements, one can partially validate the numerical scheme. This calculation is a very demanding problem for this code, since this test requires having two-phase flow at the centerline, where the equations are mildly singular. Furthermore the axisymmetric terms, which are not treated in conservation form, are very important due to the high radial velocity near the centerline.

The first test of the model was the calculation of axisymmetric bubble collapse far away from physical boundaries. For a quantitative evaluation of the code, the bubble size was plotted versus time and compared to the experimental measurements of Ohl et al. (1995). Because Ohl et al.'s data start as the bubble is collapsing, an initial velocity field was constructed from Ohl's reported initial bubble wall velocity. The liquid velocity field was initialized to a potential flow field consistent with the bubble radius and wall velocity. The results are shown in Figure 3 with the instant of collapse defined at $t=0$. The calculated collapse is slightly slower than the measured collapse, but otherwise agrees well. The slight disagreement likely comes from two sources. Firstly, the initial velocity condition was projected onto the numerical grid from the potential flow field. This projection is an imperfect fit to the discretized equations. The second reason for the disagreement is that as the bubble collapses, the resolution of the bubble becomes increasingly poor. Some of the energy of collapse is lost as the size of the bubble drops to the grid cell level. The calculation correctly predicted a strong outward compression wave after the bubble collapsed, as can be seen in Ohl et al.'s photographs. Figure 4 shows the numerical prediction of this outward moving wave. This prediction of this pressure wave is an important benefit of the consideration of liquid compressibility. It is important to note that the model underestimated bubble rebound by predicting only trace amounts of vapor instead of a fully formed bubble. This

disagreement between prediction and experimental measurement is likely a result of the energy loss as the size of the bubble shrinks below the resolvable level.

The behavior of a simple nozzle geometry was investigated in great detail. The first test was to check for grid sensitivity. The length of the nozzle in these calculations was 4.0 with a diameter of 1.0, and a minimum radius on the inlet corner of 0.025. Although some of the experimental data used for comparisons came from sharper nozzles than 0.025, it was necessary to have some rounding of the inlet corner to avoid a singularity in the transformation from physical to numerical coordinates. Grid sensitivity was checked by discretizing the same geometry with two different 140 by 40 grids. The only sensitivity noted was that the transient length of the cavitation film could change with the different grids. However the time averaged mass flow into the domain changed by only 0.4%.

For the nozzle calculations, the upstream pressure was varied over a very wide range, from a non-dimensional value of 0.075 to 1.0. The downstream pressure was held constant at 0.05. The calculations were performed on a grid of at least 140 by 40 points with a CFL number of about 1.0, based on liquid sound speed. The sound speed, rather than $a+u$, was used for estimating the CFL number because the velocity field is not known *a priori*:

$$CFL = \frac{a\Delta t}{\min(\Delta x, \Delta y)} \quad (25)$$

An image of the instantaneous flow field in one such calculation is shown in Fig. 5 for a nozzle with $L/D=4$. This image was very similar to photographs of cavitating nozzles taken by Chaves(1995). Rather than forming spherical bubbles, the cavitation region stretched out into a long film along the wall. Unfortunately, some smearing of the trailing edge of the bubble occurred, which can be seen in the density contours. For most of the length of the nozzle the liquid was constricted into a *vena contracta*. The liquid re-expanded near the nozzle exit, accompanied by an increase in pressure. The bubble extended slightly further and reached the nozzle exit. This suggested that the bubbles could collapse outside of the nozzle, as observed by Chaves.

The model also agreed with quantitative measurements of nozzle flow. The predicted coefficient of discharge was compared to experimental measurements for sharp nozzles, as shown in Fig. 6. The time-averaged coefficient of discharge was plotted versus K , a cavitation parameter which was chosen for its usefulness in collapsing cavitating nozzle data (Schmidt et al.,1995).

$$K \equiv \frac{P_0 - P_v}{P_0 - P_\infty} \quad (26)$$

The experimental data show considerable scatter, but were very close to the predicted value of C_d . As a further comparison to experimental data, the predicted centerline exit velocities were compared with experimental data from Chaves et al. (1995). These results are shown in Fig. 7 for nozzles with $L/D=10$. The model predictions agreed quite well with the experimental velocities.

Because the equations are solved on a boundary fitted mesh, the model is capable of calculating flow through a variety of geometries. The effect of varying nozzle length is shown in Figure 8. The coefficient of discharge agrees very well with experimental measurements from Ohm et al. (1991). These predictions confirm that discharge is a very weak function of length. The shape of the inlet corner was also varied. Figure 9 shows calculated results for flow through a rounded nozzle. A long, thin, cavitation region is predicted behind the inlet corner. These results suggest that at very high injection pressures even rounded nozzles are prone to cavitation. Another interesting feature of this calculation is that the flow is supersonic where the vapor reaches the exit, which could mean that a shock exists just outside the nozzle exit.

Figure 10 shows the predicted coefficient of discharge as a function of inlet corner radius. The predictions are compared with data from Ohm et al. (1991). The predicted and computed discharge agrees quite closely, with the exception of one point, at $r/D=0.2$. However, the experimental data point appears to be an outlying point from the other experimental data, possibly a result of hydraulic flip. The same experimental data point for a nozzle with $L/D=3$ is shown. As mentioned above, coefficient of discharge is known to be a very weak function of length and so the results for $L/D=3$ are likely to be similar to $L/D=4$ if neither nozzle is flipped. The measured value

from the shorter nozzle is more consistent with the other experimental data points and the predicted values.

As a further demonstration of this code, a grid was developed similar to that of Koo and Martin [1995]. They calculated the flow through an axisymmetric injector tip, including a stationary needle. However, their calculation assumed incompressibility whereas the present work includes a cavitation model. An image of the results is shown in Fig. 11 for an upstream pressure of 1.0 and a downstream pressure of 0.5. The streamlines show that the flow separates from the outer wall as the fluid enters the sac, but then reattaches near the nozzle entrance. Figure 11 also shows that the majority of the pressure drop through the tip occurs at the orifice entrance. The pressure drop across the valve seat is very small in comparison. The enlarged image of the nozzle is shown in Fig. 12. This result is very similar to the plain orifice shown in Fig. 5. The coefficient of discharge for the entire tip was 0.68, slightly higher than that of the plain orifice for the same upstream and downstream pressure. This is due to the obtuse angle between the nozzle wall and sac wall in the tip.

In nature cavitating nozzles likely shed bubbles in a non-axisymmetric fashion. However, all of the previous results shown have been made with the assumption of axisymmetry. This assumption tends to discourage any sort of shedding or regular oscillation. Not surprisingly, the transient calculations of axisymmetric nozzle flow tended to eventually stabilize. Since these oscillations could significantly enhance spray breakup, they are of great interest to the spray community. In attempt to capture some of these oscillations with a two-dimensional code, a simulation has been run of an asymmetric planar slot, as shown in Fig. 13. The length to diameter ratio is 4.2 and the radius of the inlet corner is 0.05 times the diameter. This geometry is reminiscent of a valve-covered orifice (VCO) fuel injector geometry where the left boundary would be the needle surface. In such flows the majority of fuel would be expected to come from above and considerably less fuel would come from the sac below. For this simulation, all of the mass was introduced at the upper surface and the bottom surface was made a wall. A constant upstream pressure of 1.0

(corresponding to 100 MPa) and a downstream pressure of 0.05 (corresponding to 5 MPa) was used. In this case, the flow demonstrated very large transient variations. The coefficient of discharge for the slot varied from 0.2 to 0.8. The cavity would periodically stretch to the exit and then collapse entirely, generating strong pressure waves and vortices. Figure 13 is a series of images showing the cyclic nature of cavity growth and collapse. After collapse, bubbles would pinch off the main cavity and be swept downstream during the collapse process. A new cavity would form and the process would repeat. Figure 13(a) shows the cavity during collapse. The cavity disappears completely by Figure 13(c), and then re-forms by Figure 13(h). Figures 13(i) and (j) show the cavity beginning to collapse again. The frequency at which this shedding occurred was found to be roughly 33 kHz with a value of κ of 0.05 and increased to 26 kHz when κ was increased to 0.10.

There are other differences between the axisymmetric and asymmetric results. In the axisymmetric calculations, such as in Fig. 5, the bubble stays very close to the wall. In the asymmetric case, the incoming momentum directs the liquid against the lower wall, creating a larger, more central cavitation region. The asymmetric results may be compared to the experimental work of Kim et al. (1997) who made photographic investigations of three-dimensional transparent injector tips. Kim et al. observed strong asymmetry in the cavities within nozzle holes. They noted that the cavitation region could extend to the exit of the nozzles, depending on the geometry of the tip. Arcoumanis, et al. (1998) also investigated a transparent, three-dimensional VCO nozzle. They made photographs of the cavitation in the nozzles which strongly resemble the computational results of Fig. 13.

Conclusions

A new model of cavitating flow was constructed based on the assumption of thermodynamic equilibrium. The hydrodynamic equations were closed using an algebraic equation of state that described isentropic phase change and considered compressibility of both phases. These equations

were solved on a two-dimensional boundary fitted mesh for both the collapse of a single bubble and for cavitating nozzle flow.

The results for the single bubble calculations were acceptable, and agreed closely with experimental observations of high speed nozzle flow. The model accurately predicted quantifiable characteristics of nozzle flow such as coefficient of discharge and centerline velocity at the nozzle exit for sharp nozzles. Some smearing of the collapse region was observed, as is typical of continuum schemes. Future work involving better numerical treatment of the interface may remedy this limitation. The cavitation model also predicted the flow through an axisymmetric nozzle tip. In this case the results were quite similar to the plain orifice flow. However the calculated behavior of flow through an asymmetric nozzle were considerably different than through a plain orifice. The asymmetric flowfield tended to exhibit strong transients which would have a dramatic influence on spray breakup.

Acknowledgments

This material is based upon work supported by the U.S. Army Research Office under grant No. DAAH04-94-G-0328.

References

- Arcoumanis, C., M. Gavaises, J. M. Nouri, E. Abdul-Wahab, and Roy. W. Horrocks, "Analysis of the Flow in the Nozzle of a Vertical Multi Hole Diesel Engine Injector," SAE Paper 980811, 1998.
- Avva, Ram K., Ashok Singhal, Dennis H. Gibson. "An Enthalpy Based Model of Cavitation." ASME FED v. 226, pp. 63-70, 1995.
- Bergwerk, W., "Flow Pattern in Diesel Nozzle Spray Holes," *Proceedings of the Institute of Mechanical Engineers*, vol. 173, pp. 655-660, 1959.

- Chaves, H. et al., "Experimental Study of Cavitation in the Nozzle Hole of Diesel Injectors Using Transparent Nozzles," SAE Paper No. 950290, pp. 199-211, 1995.
- Chen, Yongliang, and Stephen D. Heister, "Two-Phase Modeling of Cavitated Flows," *Computers and Fluids*, v. 24, n. 7, pp. 799-809, 1995
- Chen, Yongliang, and Stephen D. Heister, "A Numerical Treatment for Attached Cavitation," *J. of Fluids Engineering*, vol. 116, n. 3, pp. 613-618, 1994.
- Delannoy, Y., Modélisation d'écoulements instationnaires et cavitants. INPG Doctoral Thesis, Grenoble, July, 1989.
- Delannoy, Y. and J. L. Kueny, "Two Phase Flow Approach in Unsteady Cavitation Modeling," *Cavitation and Multiphase Flow Forum*, ASME FED vol. 98, pp. 153-158, 1990.
- Gelalles, A. G., "Coefficients of Discharge of Fuel Injection Nozzles for Compression-Ignition Engines," NACA Technical Memo. 373, pp. 193-209 1931.
- He, Lu, and Francisco Ruiz, "Effect of Cavitation on Flow and Turbulence in Plain Orifices for High-Speed Atomization," *Atomization and Sprays*, v. 5, pp. 569-584, 1995.
- Hiroyasu, H., M. Arai, and M. Shimizu, "Break-Up Length of a Liquid Jet and Internal Flow in a Nozzle," ICLASS-91 Gaithersburg, MD, pp. 275-282, July 1991.
- Hyman, James M., "Numerical Methods for Tracking Interfaces," Los Alamos National Laboratory Rept. LA-9917-MS, 1984, pp. 1-20.
- Kato, H. and H. Kayano, and Y. Kageyama, "A Consideration of Thermal Effect on Cavitation Bubble Growth," *Cavitation and Multiphase Flow*, ASME F.E.D. vol. 194, 1994.
- Kim, J. H., K. Nishida, and H. Hiroyasu, "Characteristics of the Internal Flow in a Diesel Injection Nozzle," ICLASS-97, Seoul, 1997, pp. 175-182.
- Knapp, Robert T., James W. Daily, Frederick G. Hammitt. *Cavitation*. McGraw-Hill, p. 94, 1970.
- Knox-Kelecy, Andrea L. and Patrick V. Farrell, "Internal Flow in a Scale Model of a Diesel Fuel Injector Nozzle," SAE Paper No. 922308, pp. 1-7, 1992.
- Koo, Ja Ye and Jay K. Martin, "Near-Nozzle Characteristics of a Transient Fuel Spray," *Atomization and Sprays*, vol. 5, n.1, 1995.

- Kubota, A., H. Kato, and H. Yamaguchi, "Finite Difference Analysis of Unsteady Cavitation on a Two-Dimensional Hydrofoil," *Proc. of the 5th Int. Conf. on Numerical Ship Hydrodynamics*, Hiroshima, pp. 667-683, Sept. 1989.
- Ohl, C.-D., A. Philip, W. Lauterborn, "Cavitation Bubble Collapse Studied at 20 Million Frames per Second," *Annalen der Physik*, v. 4, n. 1, pp. 26-34, 1995.
- Ohrn, T. R., D. W. Senser, and A. H. Lefebvre, "Geometric Effects on Spray Cone Angle for Plain-Orifice Atomizers," *Atomization and Sprays*, vol. 1, pp. 137-153, 1991.
- Poinsot, T. J., and S. K. Lele, "Boundary Conditions for Direct Simulations of Compressible Viscous Reacting Flows," *J. of Computational Physics*, v. 101, pp. 104-129, 1992.
- Reitz, Rolf Deneys, *Atomization and Other Breakup Regimes of a Liquid Jet*, Ph.D. thesis, Princeton Univ., p. 163, 1978.
- Rider, William J., and Douglas B. Kothe, "Stretching and Tearing Interface Tracking Methods," Los Alamos National Laboratory Report LA-UR-95-1145, 1995, pp. 1-11.
- Schmidt, D., T.-F. Su, K. Goney, P. V. Farrell, and M. L. Corradini, Detection of Cavitation in Fuel Injector Nozzles in S. H. Chan (ed.), *Transport Phenomena in Combustion*, Taylor and Francis, vol. 2, p. 1521, 1996.
- Soteriou, Celia, Richard Andrews, and Mark Smith, "Direct Injection Diesel Sprays and the Effect of Cavitation and Hydraulic Flip on Atomization," SAE Paper No. 950080, p. 27-51, 1995.
- Thompson, Kevin W., "Time Dependent Boundary Conditions for Hyperbolic Systems," *J. of Computational Physics*, v. 68, p. 1-24, 1987.
- Wallis, Graham, B., *One-dimensional Two-phase Flow*. McGraw-Hill. p. 143, 1969.
- Zijlema, M., "On the Construction of a Third-Order Accurate Monotone Convection Scheme with Application to Turbulent Flows in General Domains," *Int. J. for Numerical Methods in Fluids*, v. 22, pp. 619-641, 1996.

Nomenclature

a	sound speed
C_d	coefficient of discharge
D	nozzle diameter
h	enthalpy
i, j	indices in the η, ζ directions
k	thermal conductivity
K	a cavitation parameter used in nozzle flow
ℓ_1	the wave which is coming from outside the domain in subsonic flow
L	the length of the nozzle, also enthalpy of vaporization
p	pressure
r	radius of curvature of the inlet corner
R_I	radius of a bubble whose growth is controlled by inertial effects
R_T	radius of a bubble whose growth is controlled by thermal effects
r, z	spatial location in polar coordinates
u, v	velocity in the x and y direction
x, y	spatial location in Cartesian coordinates

Greek

α	void fraction
η, ζ	computational coordinates
κ	constant of proportionality used in the exit boundary condition
μ	viscosity
Φ	viscous energy dissipation
ρ	density
ω	zero in Cartesian coordinates, unity in polar coordinates
τ	shear stress

Subscripts

<i>exit</i>	at the nozzle exit
<i>g</i>	vapor
<i>in</i>	at the nozzle inlet
<i>l</i>	liquid
<i>sat</i>	at saturation
<i>v</i>	viscous
<i>0</i>	far upstream of the nozzle
∞	far downstream of the nozzle

Figure Captions

1. Barotropic equations of state on log-log axes: The solid line is the same type used by Delannoy and Kueny but with a density ratio of ten-thousand to one. The dashed line is the equation of state used in this study and is based on the assumptions of homogenous equilibrium.
2. Typical physical and computational domain for nozzle calculations: The top sketch is the physical domain and the bottom is the corresponding computational domain.
3. This figure shows a comparison of the predicted and measured collapse of a single spherical bubble from Ohl et al. (1995). The time datum, $t=0$, is defined at the moment of bubble collapse.
4. After the bubble collapse, a strong high pressure wave emanates from the bubble center. This wave significantly compresses the liquid. These frames show calculated densities at eight successive points in time. Saturated liquid densities are white and higher densities are dark. A very strong, high pressure wave is formed after collapse, as shown in Frame (a). In successive Frames (b) through (h) the wave expands and weakens. Ohl et al. (1995) has observed this type of wave photographically.
5. Output at a single point in time for cavitating flow with a sharp nozzle inlet: The inlet pressure is 1.0, and the downstream pressure is 0.05 with an inlet corner radius of 0.025 and $L/D=4$. The upper half of the figure shows five density contours ranging from zero to one. The lower half shows every 10th momentum vector in the η direction and every 5th momentum vector in the ξ direction.
6. Comparison of experimental and predicted coefficient of discharge for flow through a sharp nozzle with an L/D of 4.0.

7. Comparison of predicted centerline velocity and measurements by Chaves et al (1995) at the exit of a nozzle with $L/D=10$ and sharp inlet corners.
8. Comparison of predicted and measured discharge for varying nozzle length. The numerical model had an inlet corner radius of $r/D=0.05$. The nozzle used in Ohrn et al. (1991) had as sharp a corner as could be manufactured.
9. Output at a single point in time for cavitating flow with a rounded nozzle inlet: The inlet pressure is 0.7, and the downstream pressure is 0.05 with an inlet corner radius of 0.25. The upper half of the figure shows five density contours ranging from zero to one. The lower half shows every 10th momentum vector in the η direction and every 5th momentum vector in the ξ direction.
10. Comparison of predicted and measured discharge for varying inlet corner radius. Experimental data are from Ohrn et al. (1991). All nozzles had an L/D of 4 except where noted.
11. Calculation of flow through an axisymmetric nozzle tip. The left side of the figure shows streamlines and the right side shows non-dimensional pressure. The needle surface is rendered by artificial shading.
12. Calculated momentum vectors and density field in the nozzle of the axisymmetric tip. For clarity, not all vectors are shown.
13. Calculation of asymmetric flow through a planar slot. Flow enters from the upper left and exits at the lower right side of the figure; all other boundaries are walls. The images are 2.86 microseconds apart. The dark regions in the figures are low density, and the profile at the exit of the nozzle shows exit momentum. These calculations were done with $\kappa=0.05$.

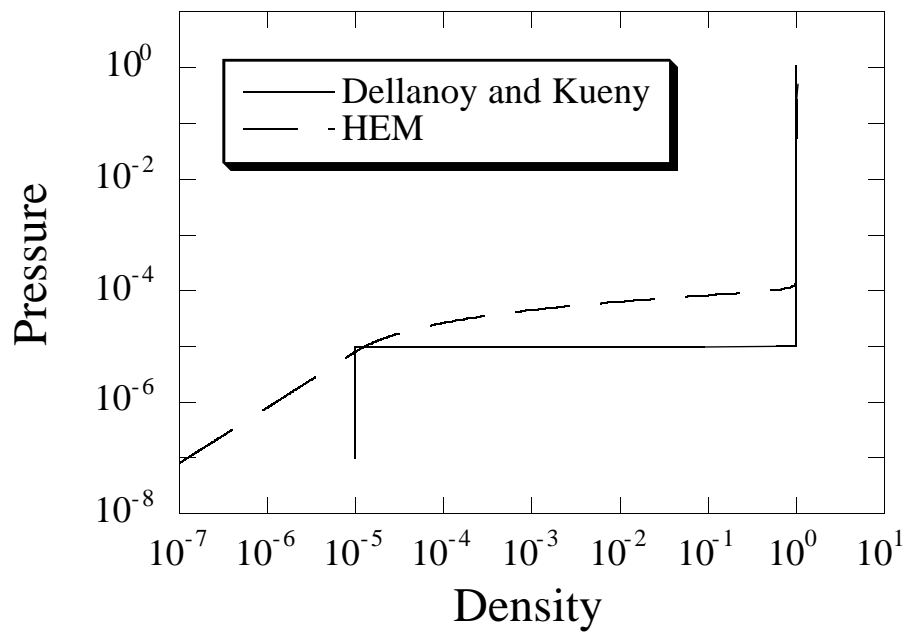


Figure 1

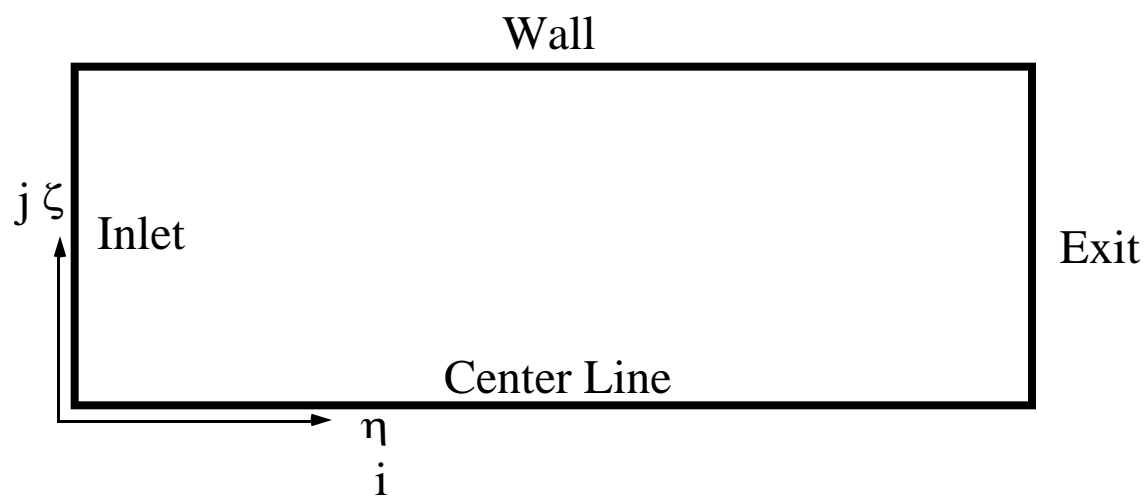
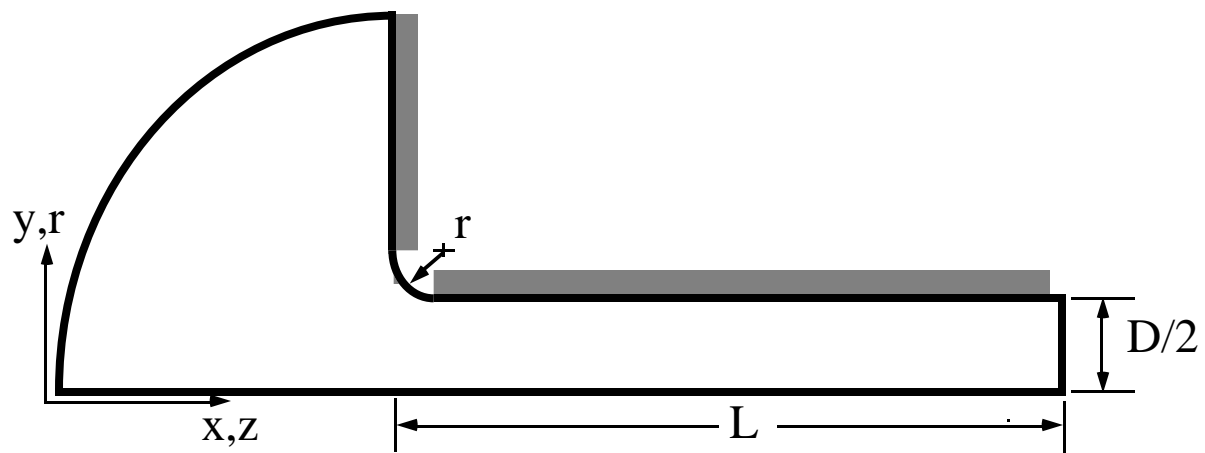


Figure 2

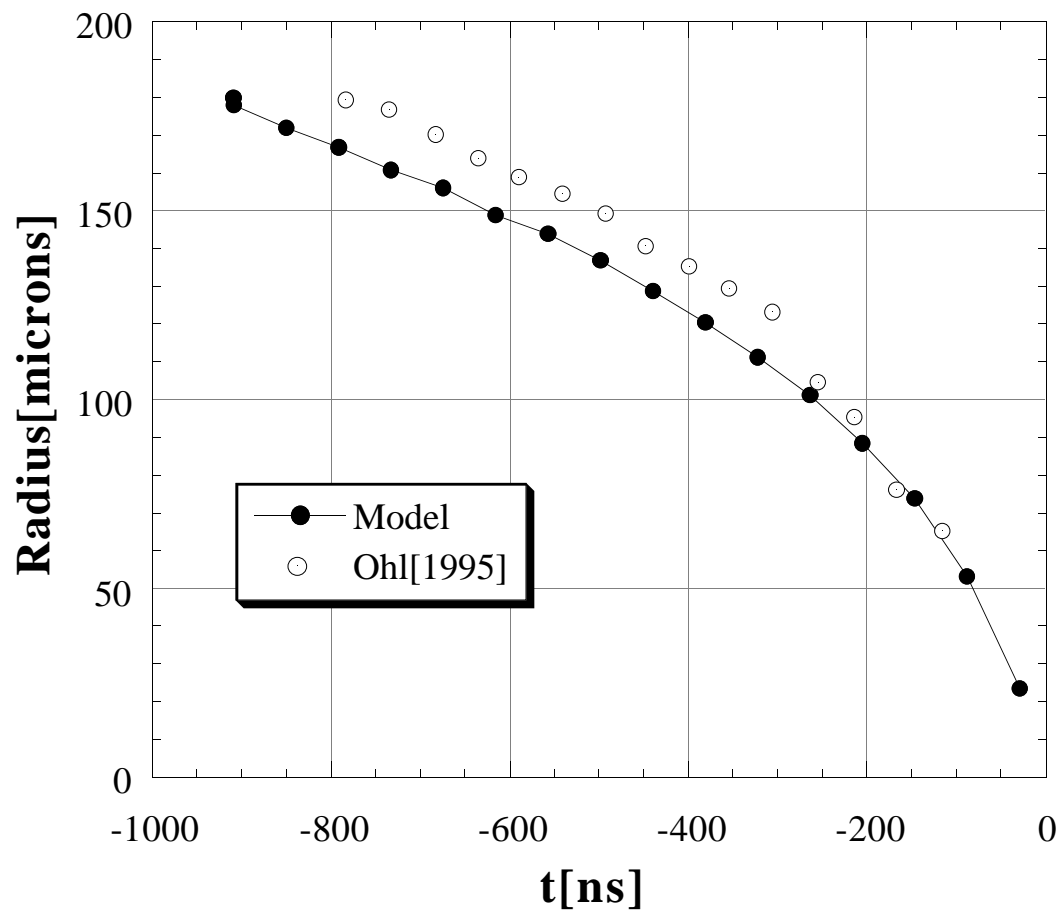


Figure 3

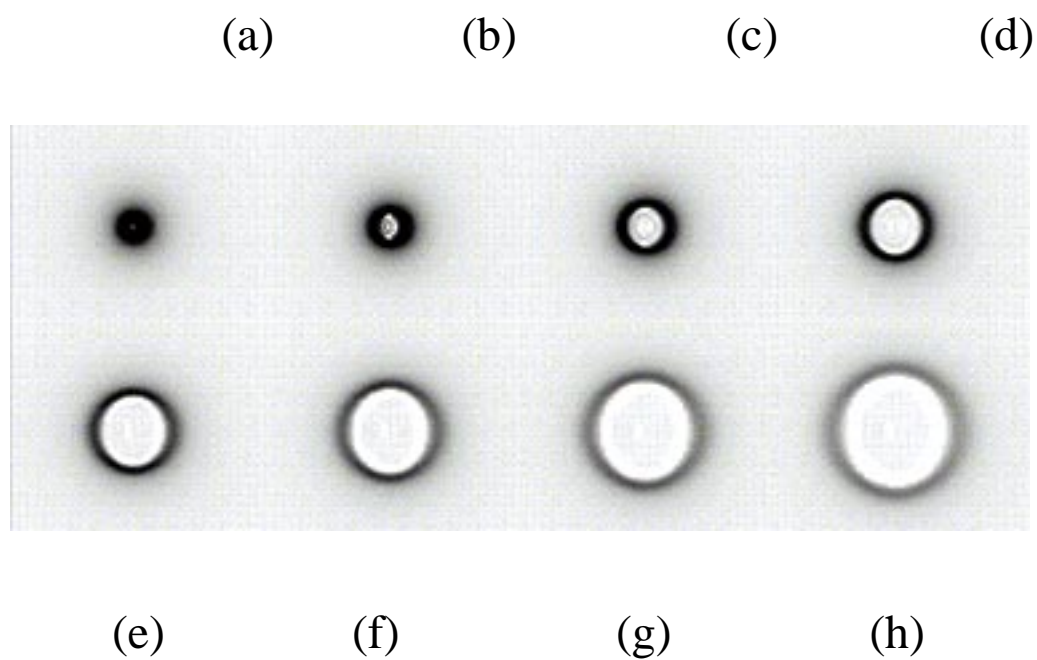


Figure 4

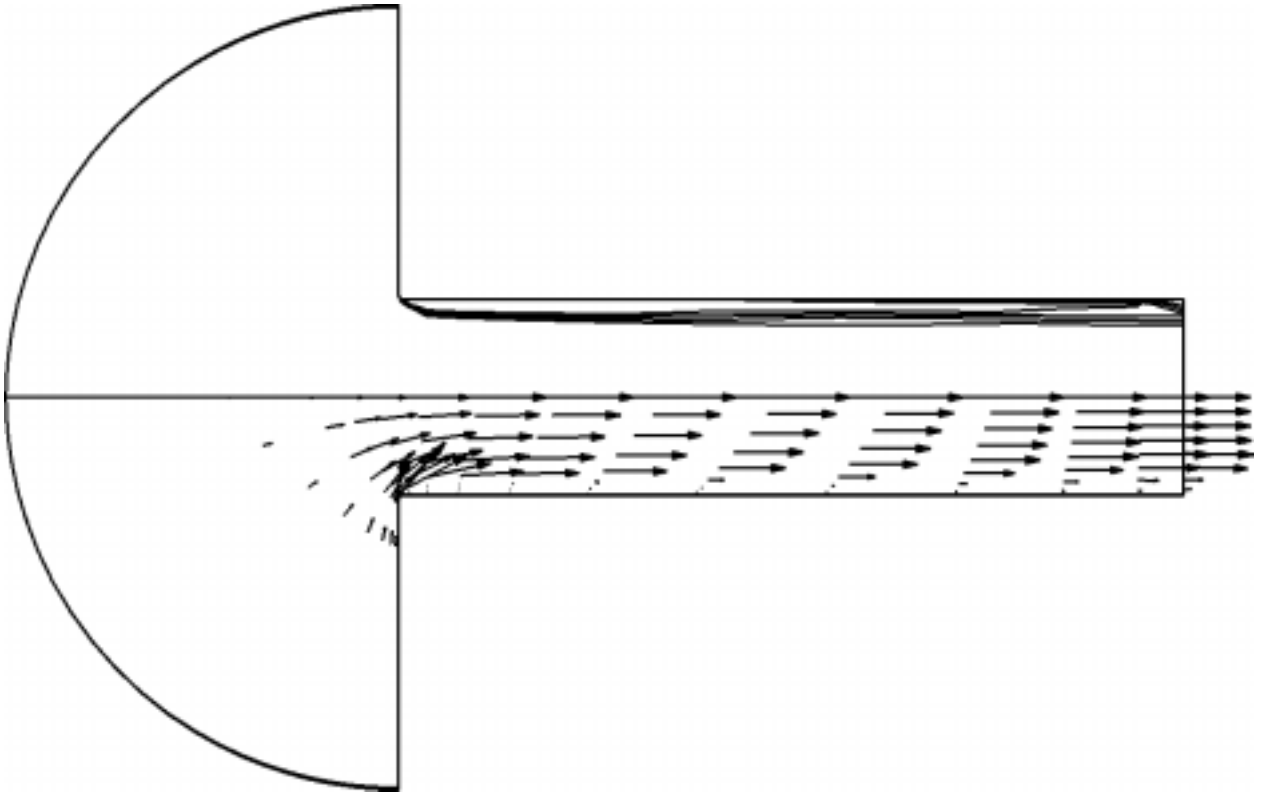


Figure 5

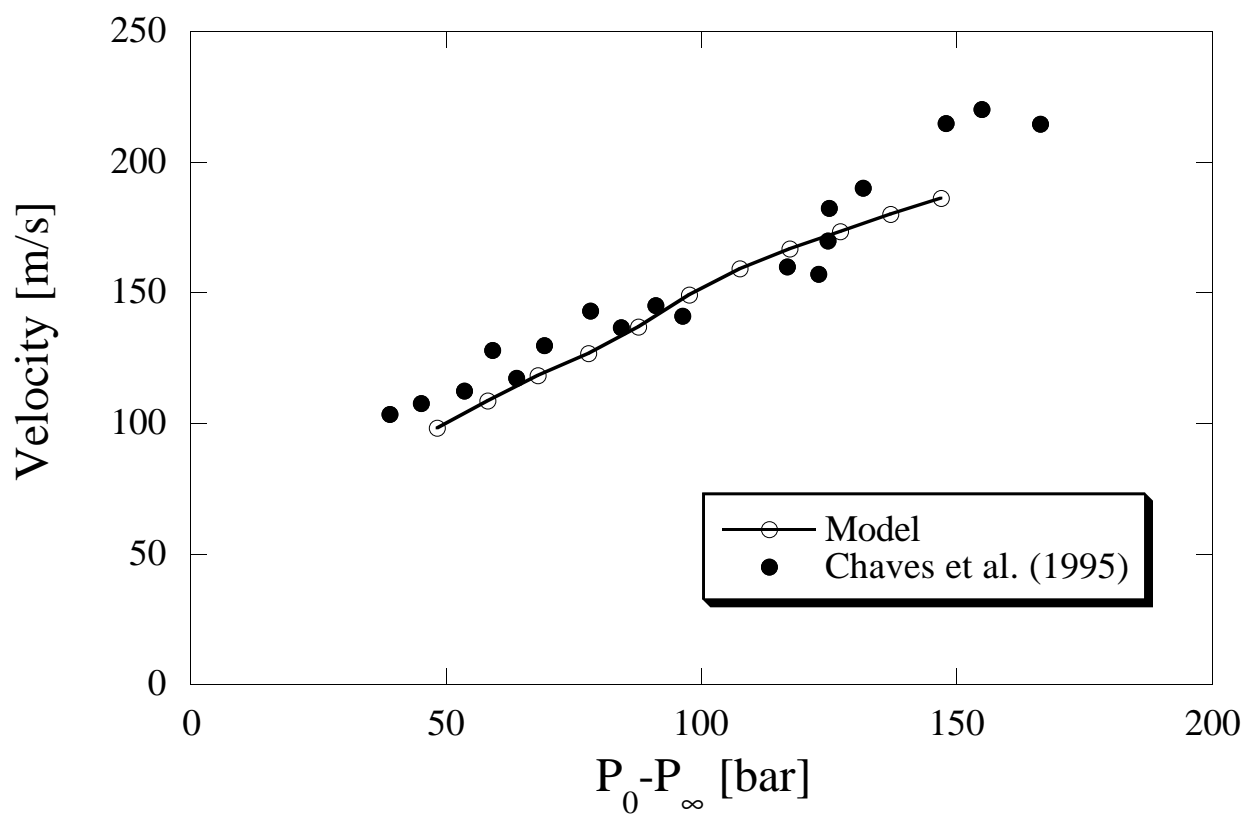


Figure 7

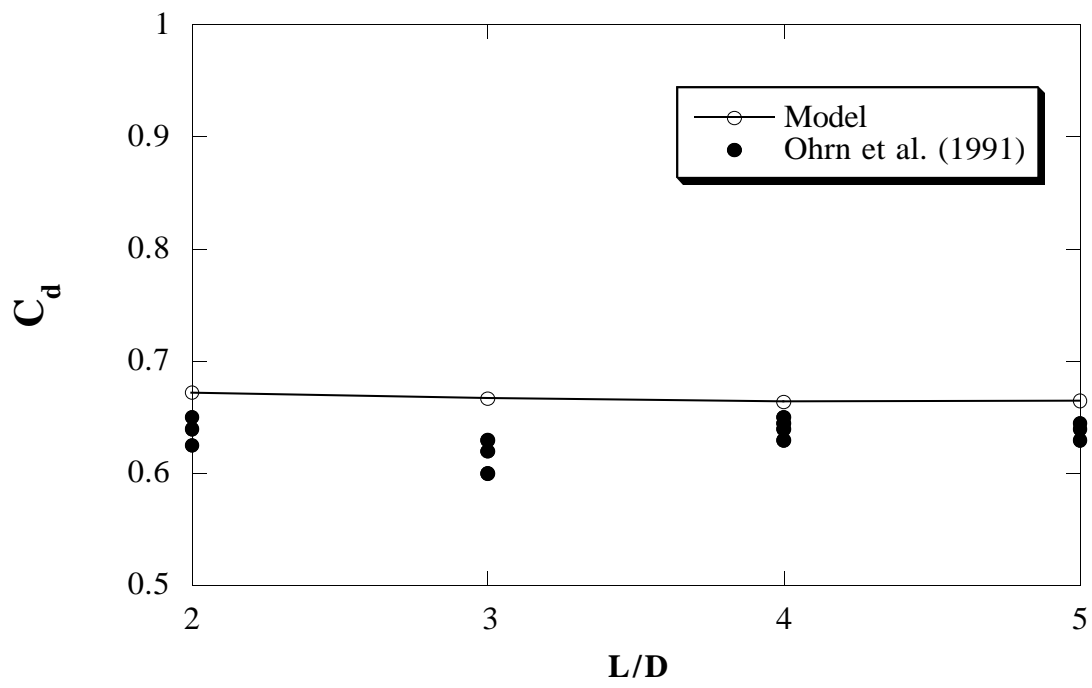


Figure 8

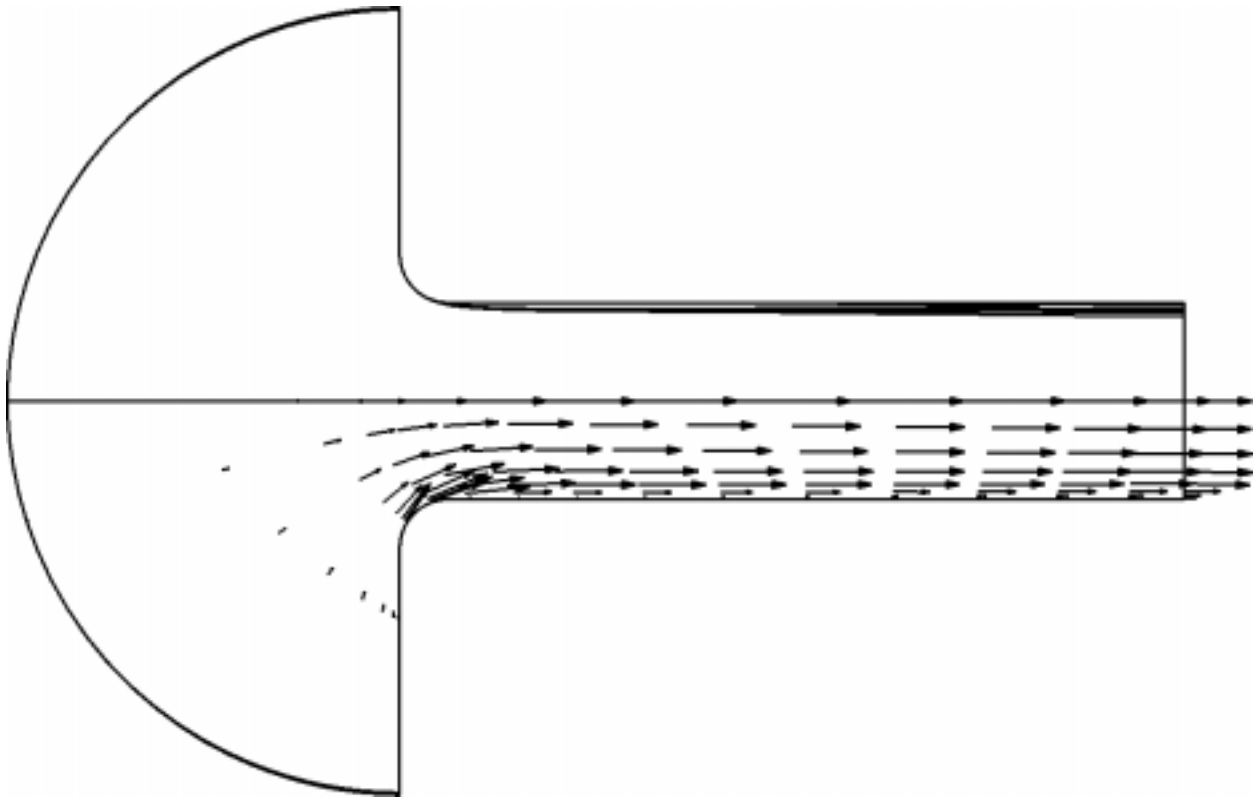


Figure 9

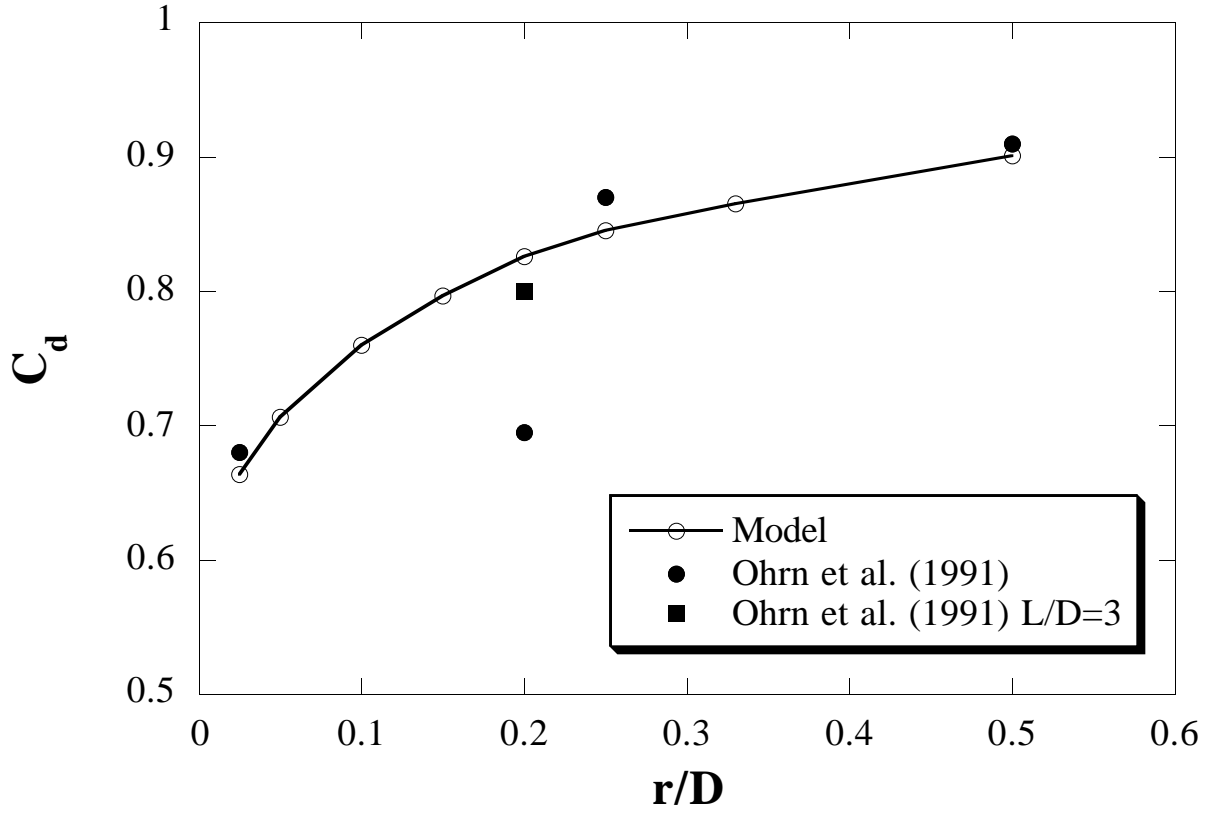


Figure 10

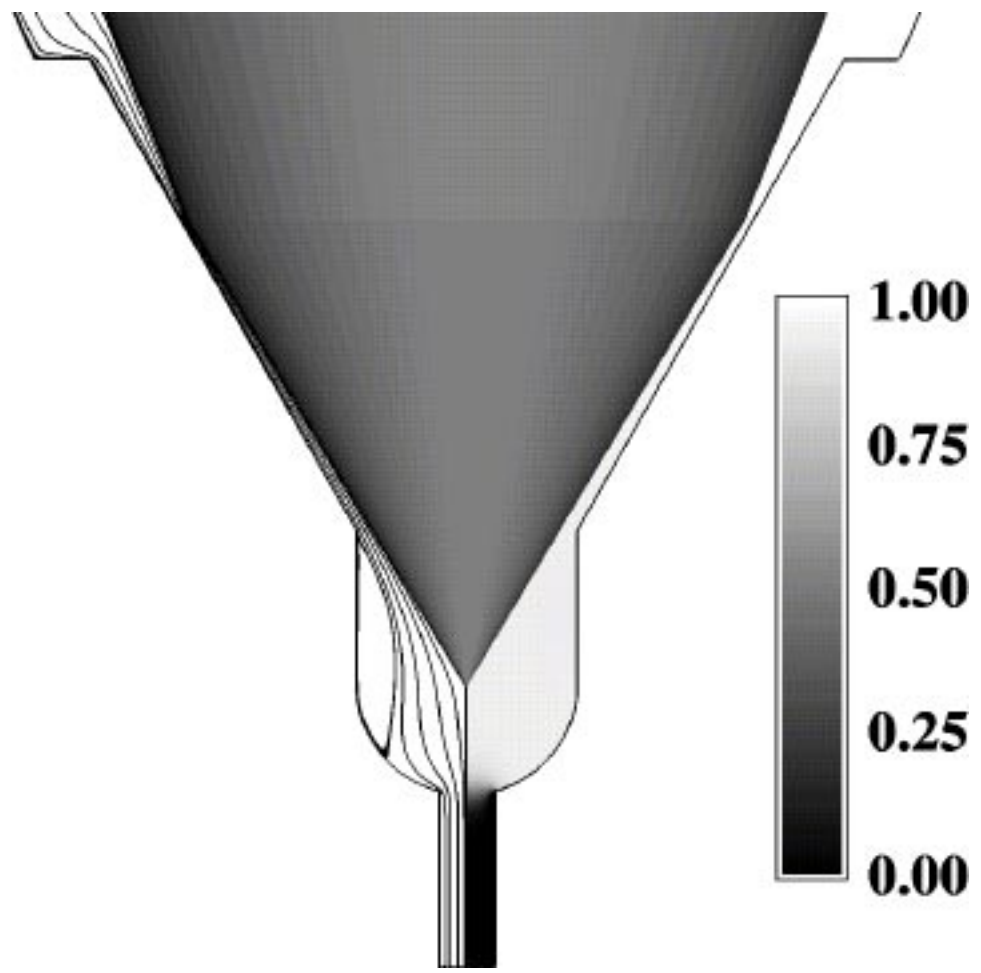


Figure 11

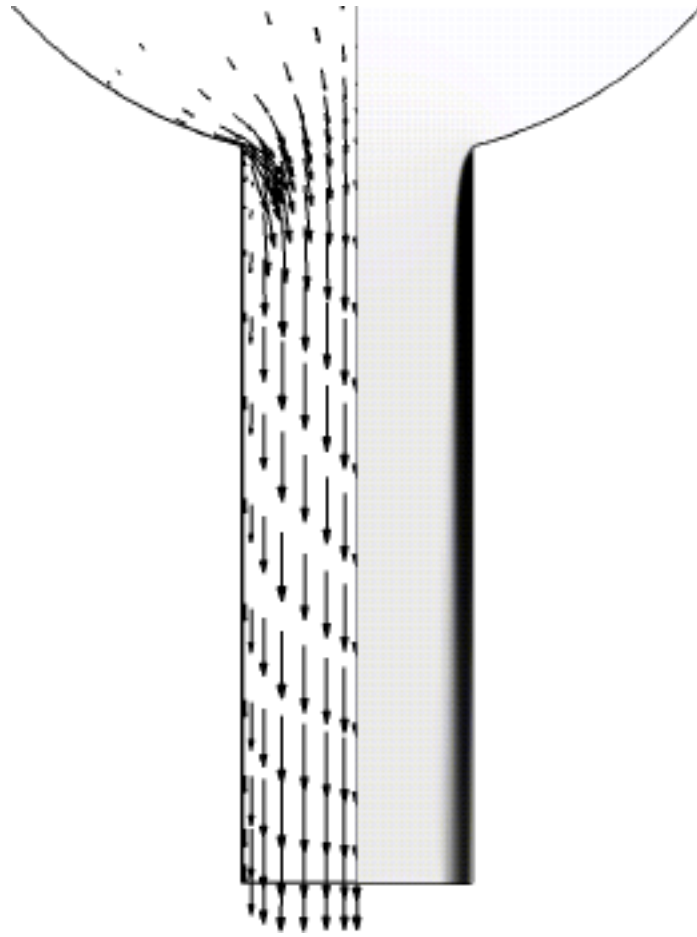


Figure 12

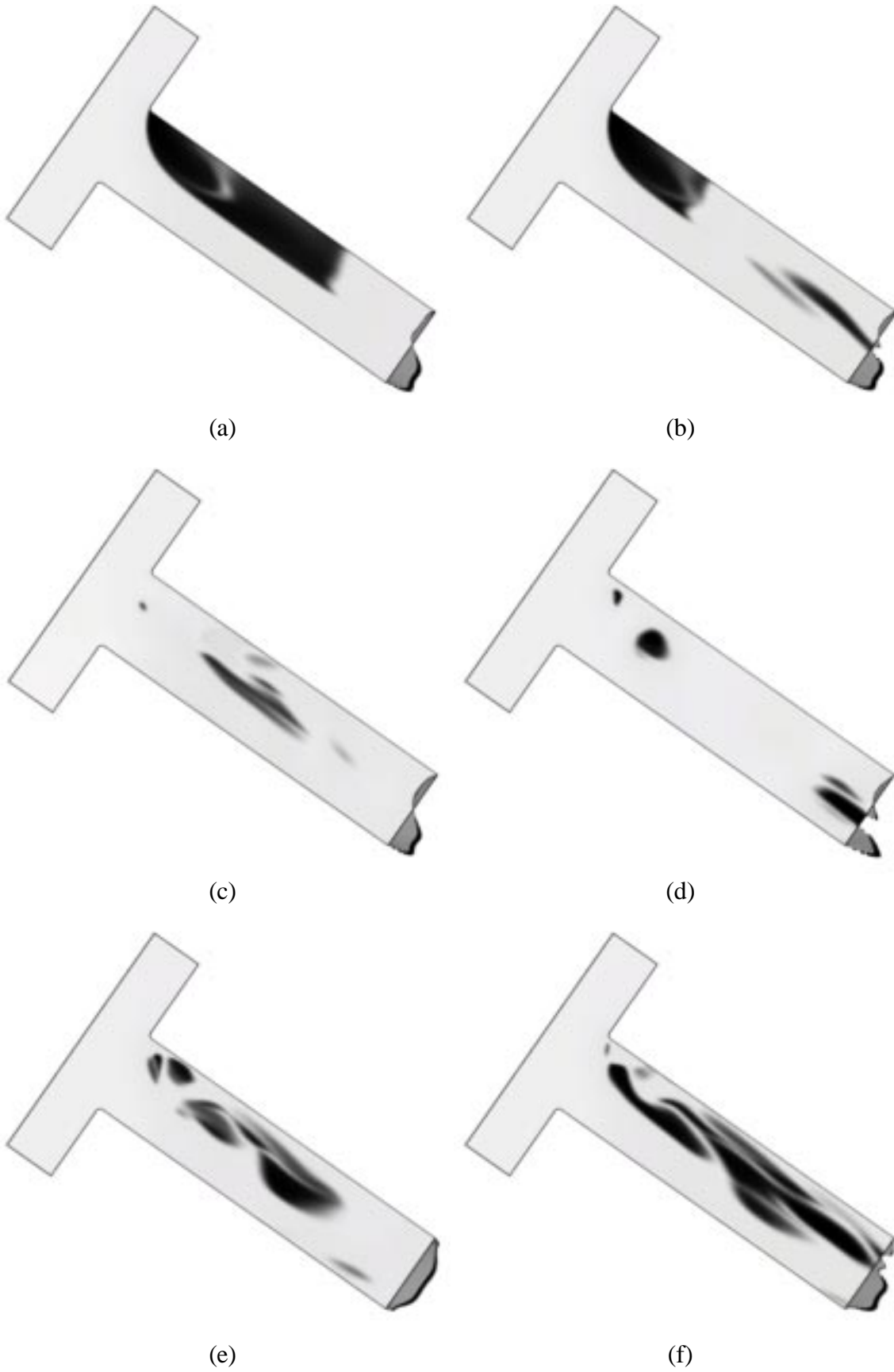


Figure 13

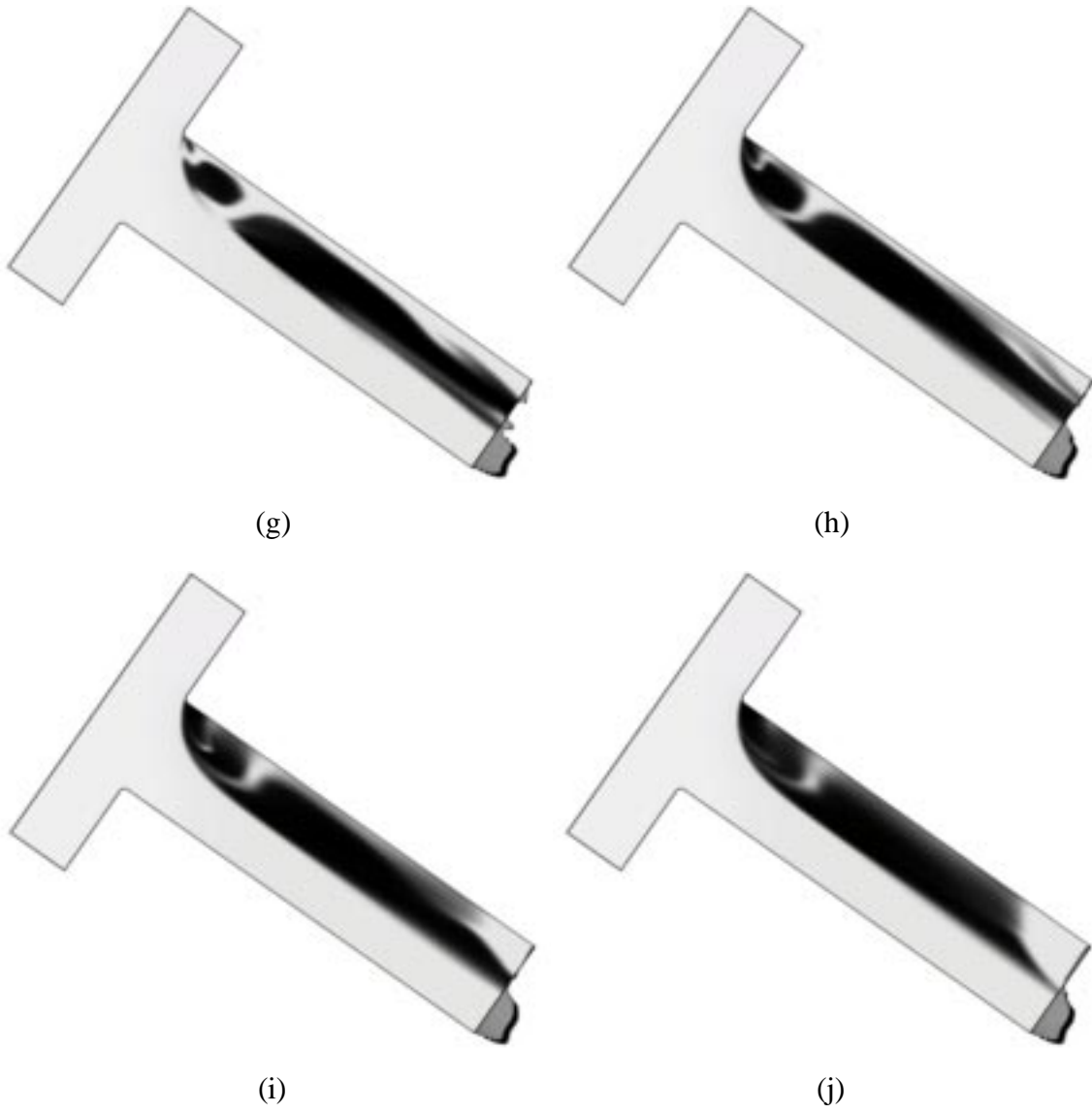


Figure 13, continued